



This is a repository copy of *Continuum and atomistic description of excess electrons in TiO<sub>2</sub>*.

White Rose Research Online URL for this paper:  
<http://eprints.whiterose.ac.uk/91418/>

Version: Accepted Version

---

**Article:**

Maggio, E., Martsinovich, N. and Troisi, A. (2016) Continuum and atomistic description of excess electrons in TiO<sub>2</sub>. *Journal of Physics: Condensed Matter*, 28 (7). ISSN 0953-8984

<https://doi.org/10.1088/0953-8984/28/7/074004>

---

**Reuse**

Unless indicated otherwise, fulltext items are protected by copyright with all rights reserved. The copyright exception in section 29 of the Copyright, Designs and Patents Act 1988 allows the making of a single copy solely for the purpose of non-commercial research or private study within the limits of fair dealing. The publisher or other rights-holder may allow further reproduction and re-use of this version - refer to the White Rose Research Online record for this item. Where records identify the publisher as the copyright holder, users can verify any specific terms of use on the publisher's website.

**Takedown**

If you consider content in White Rose Research Online to be in breach of UK law, please notify us by emailing [eprints@whiterose.ac.uk](mailto:eprints@whiterose.ac.uk) including the URL of the record and the reason for the withdrawal request.



[eprints@whiterose.ac.uk](mailto:eprints@whiterose.ac.uk)  
<https://eprints.whiterose.ac.uk/>

# Continuum and atomistic description of excess electrons in TiO<sub>2</sub>

Emanuele Maggio,<sup>1,\*</sup> Natalia Martsinovich<sup>1,2</sup> and Alessandro Troisi<sup>1</sup>

<sup>1</sup> Department of Chemistry and Centre for Scientific Computing,  
University of Warwick, Coventry CV4 7AL, United Kingdom

<sup>2</sup>Department of Chemistry, University of Sheffield, Sheffield S3 7HF, United Kingdom

\*Current address: Faculty of Physics and Centre for Materials Science,  
University of Vienna, Sensengasse 8/12, A-1090 Vienna, Austria

E-mail: emanuele.maggio@univie.ac.at, n.martsinovich@sheffield.ac.uk

## Abstract

The modelling of an excess electron in a semiconductor in a prototypical dye sensitised solar cell is carried out using two complementary approaches: atomistic simulation of the TiO<sub>2</sub> nanoparticle surface is complemented by a dielectric continuum model of the solvent-semiconductor interface. The two methods are employed to characterise the bound (excitonic) states formed by the interaction of the electron in the semiconductor with a positive charge opposite the interface. Density-functional theory calculations show that the excess electron in TiO<sub>2</sub> in the presence of a counterion is not fully localised but extends laterally over a large region, larger than system sizes accessible to DFT calculations. The numerical description of the excess electron at the semiconductor-electrolyte interface based on the continuum model shows that the exciton is also delocalised over a large area: the exciton radius can have the values from tens to hundreds of Ångströms, depending on the nature of the semiconductor (characterised by the dielectric constant and the electron effective mass in our model).

## 1. Introduction

Excess electrons in semiconducting oxides play a role in many processes, from dye-sensitised solar cells (DSSC) to photocatalysis and electron transport within nanostructured films. In particular, DSSCs harvest solar radiation thanks to a chromophore adsorbed on the surface of a photoanode made of semiconductor (e.g. TiO<sub>2</sub>) nanostructures (nanoparticles or others). The chromophore, upon photoexcitation, injects an excess electron into the TiO<sub>2</sub> conduction band (CB) (this step competes with the quenching of the excited state by thermal relaxation to the dye ground state or singlet-triplet conversion). The interaction of the injected electron with the oxidised molecule across the semiconductor surface generates a charge transfer exciton (CTE) [1] [2]. The CTE can subsequently dissociate into free charge carrier in the semiconductor and localised hole on the chromophore or otherwise recombine with the oxidised dye or another electron acceptor species present in solution. To generate electricity, the free charge carrier then migrates across the semiconductor substrate [3] to the external circuit, and finally reaches the counter-electrode to promote the regeneration of the active electrolyte species and to regenerate the photoactive component.

Thus, a charge transfer exciton at the interface between the semiconductor and the electrolyte solution is one of the key structures in DSSCs: a positive dye cation is always present in the process of charge injection and recombination in DSSC; there is also the interaction between excess electrons in the semiconductor and ions in the electrolyte solution. Therefore knowing about their electronic states is a prerequisite for studying the interface

charge dynamics. Excess electrons and CTEs are also important in such applications as photocatalysis where photogenerated electrons and holes are transferred to donor and acceptor species [4] [5], and in biosensors where the semiconductor is in contact with an electrolyte solution [6]. In all these cases it is important to know if there are surface trap states induced by the presence of the ions.

CTEs are important beyond the semiconductor-electrolyte interfaces and can be found, for example, in organic photovoltaics [7]. We note that the situation is somewhat different in perovskite solar cells: free charge carriers rather than excitons were found to dominate in photoexcited perovskites [8]. The effective masses for both electron and hole in lead halide perovskites are very small [9], suggesting that the positive charge left on the perovskite may not be localised enough to sustain a charge transfer exciton.

The interaction between excess electrons in the semiconductor and ions in solution has been proposed as a possible origin for shallow trap states exponentially distributed below the CB minimum [10]. Shallow traps were reported to occur in anatase but not in rutile [11], which was tentatively assigned to differences in solvent (water) adsorption on these polymorphs' surfaces. Other proposed explanations for the microscopic origin of these states are: the presence of surface states [3], step edges [12], the effect of the material morphology (crystalline or nanoporous) [13]. The role of grain boundaries is also acknowledged, especially in ZnO based photoelectrodes, where significant differences in electron diffusion have been measured between nanoparticles and nanorods [14]. However, there is no consensus on the behaviour of grain boundaries in TiO<sub>2</sub>. Grain boundaries were dismissed as possible electron traps in DSSC photocurrent studies [15] [16]: electron transport was found to be equally fast in TiO<sub>2</sub> nanoparticles, nanorods and single crystal rutile, suggesting that transport is not controlled by grain boundaries but by surface traps. On the other hand, a recent study [17] found a strong effect of size of TiO<sub>2</sub> nanocrystals on electron transport and attributed this to the effect of grain boundaries (internal surfaces) on electron mobility. A recent computational study [18] also showed that grain boundaries can act as electron trapping sites. A study of electron transport in Nb-doped anatase [19], however, suggested that grain boundaries affect electron mobility only at low concentrations of excess electrons.

The shallow trap states are typically characterised by impedance measurements of the whole device that give an energy interval for the trap distribution between 0.09 eV and 0.14 eV below the CB minimum [3] [20] [21]. To a large extent, the spatial extension of these shallow trapped electronic states has been elusive experimentally, first because there is no universal consensus on their microscopic origin, and second because no direct on-site measurement for the photoelectrode's surface charge has been carried out to date for a device in working conditions [22]. Spectroscopic studies point to two types of electron traps in anatase: localised deep states (Ti<sup>3+</sup>) and delocalised shallow states [11] [23]. However, shallow states at 0.12-0.3 eV below the conduction band minimum were also described as localised centres [24]. Moreover, electron paramagnetic resonance (EPR) studies suggest that excess electrons are localised in rutile but delocalised in anatase [25]; two types of Ti<sup>3+</sup> sites were identified by EPR in anatase: localised and delocalised over several Ti atoms [26].

A lot of theoretical effort has been dedicated to excess electrons in  $\text{TiO}_2$ , but the majority of these studies addressed excess electrons caused by the presence of oxygen vacancies [27] [28] [29] [30] [31] [32] [33] [34] [35] [36], surface hydroxyls [29] [32] [37] or dopants, such as Nb, Ta [29] [38] [39] [40] [41], Ce, Zr [42], non-metal dopants such as N [43], B, C and F [44]. These defects were shown to give rise to deep states in the band gap, with the excess electrons localised near the oxygen vacancies or dopants in rutile [27] [31] [32] [42] [36]. Localised and delocalised arrangements are close in energy for oxygen vacancy in anatase [28] [29] [35] [36], and the results are very method-dependent: hybrid density-functional theory (DFT) of DFT+U calculations with large values of U are needed to achieve deep states (which agree with experiment) and localised solutions; both triplet [29] [35] and singlet [36] state were suggested as the lowest-energy states. Notably, qualitatively different electronic properties are observed in n-type rutile and anatase doped by pentavalent ions ( $\text{Nb}^{5+}$  and  $\text{Ta}^{5+}$ ): rutile remains a semiconductor, with new states placed in the gap and excess electron localised on Ti atoms near the dopant [39] [40] [41], while anatase becomes a conductor, with excess electron in delocalised CB states [40] [41] or in shallow donor states just below the CB [39] [40]. Although recent calculations clearly show the conducting properties of Nb- or Ta-doped anatase, the calculated localisation of the excess electron is different in different studies: electrons delocalised over all Ti atoms in a simulation cell [39] [41] or only over 4 nearby Ti atoms [40].

There have been fewer computational studies of the behaviour of excess electron in defect-free  $\text{TiO}_2$  (where typically one excess electron was added to the simulation cell, together with neutralising background charge) and there is less consensus on the degree of localisation of the electron, especially for anatase [37] [37] [45] [46] [47] [48] [49] [50]. Computational studies predict localisation in bulk rutile [48] and at subsurface sites in rutile (110) slabs [45]; localisation at either surface or subsurface sites was found favourable, depending on the crystallographic orientation of the surface [50]; alternatively, both localised (the ground state) and delocalised structures were found possible in rutile, the delocalised solution being in better agreement with experimental electron mobilities [46]. As for anatase, localisation on Ti atoms was reported in anatase bulk and in (101) slabs [37] but delocalisation (i.e. localisation over a large area, over 10-15 Å in diameter) was reported in another study [49]. Other suggestions for the location of excess electrons in stoichiometric  $\text{TiO}_2$  include: localisation at the edges between (101) and (100) facets of large anatase nanoparticles [51]; localisation at undercoordinated Ti atoms at the rutile-anatase interface in mixed-phase systems [52], trapping of electrons at step edges in anatase (101) [53]. Most relevant to the subject of semiconductor-electrolyte interface, rutile nanoparticles surrounded by electrolyte and by metal cations were found to have shallow surface trapping states [54].

In this article we investigate the structure of the charge-transfer exciton formed by excess electron in a semiconductor and a positive charge next to the semiconductor surface. To approach the study of this physical system we are going to use two complementary descriptions of the interface: atomistic (electronic structure calculations) and continuum model. In the atomistic model, a potassium ion is used as a generalised representation of a positive charge (i.e. both of metal cations present in the electrolyte, and positively charged dye molecules formed after electron injection). If we find delocalised states with potassium

ion then it is likely that any larger ion or an ion further away from the surface would cause delocalised states. We want to find out if slab models of computationally accessible size can describe correctly charge-transfer exciton near the surface.

Explicit atomistic simulations of the  $\text{TiO}_2$  surface interacting with a positively charged counterion are presented in section 2. In section 3 we adopt a continuum representation with the electron and a point-like positive charge embedded in two dielectric media of different (static) dielectric constant. A numerical solution to this effective one-body quantum problem is discussed in section 3.3. We show that a trap state for the excess electron can be obtained if the Coulomb interaction across the interface is taken into account; our results relate well with the experimental energy window for a reasonable choice of model parameters and allow us to evaluate the spatial extension of the excess electron in the semiconductor's CB. The two approaches corroborate each other's findings and point to an excitonic trap state which is delocalised over a large area.

## 2. DFT simulations of excess electron in $\text{TiO}_2$ slabs

### 2.1. Method

Density-functional theory calculations of  $\text{TiO}_2$  anatase and rutile slabs containing excess electrons were done using CRYSTAL09 software [55] [56] with all-electron description of  $\text{TiO}_2$  and K, with triple valence plus polarisation basis sets for Ti, O and K (86-411(d31) basis for Ti, 8-411d1 for O, 86-511G for K [57] [58] [59]), with a  $2 \times 2 \times 1$  Monkhorst-Pack grid of k-points, using the B3LYP hybrid density functional [60] [61]. The hybrid functional was used in order to avoid unphysical delocalisation of excess electron produced by pure DFT (generalised gradient approximation-GGA) functionals [27] [38] and to avoid the uncertainty in the choice of the U value in a DFT+U scheme [34] [47] [62]. (The value of Hubbard parameter U in literature studies is either calculated "from first principles" [63] [47] or fitted to reproduce some property, such as the energy of a defect level [45] [30], or a range of U values can be scanned [34] [28] [45] [62] [40]. Therefore, different authors recommend different optimal values of U, from 4.0 to 5.8 eV [28] [45] [40], and even as low as 2-3 eV if energies of redox reactions are the property to be reproduced [34].) The B3LYP functional used here has been widely used for calculations of semiconductors, including  $\text{TiO}_2$  [28] [29] [37] [62]. The computational setup used in this work is similar to our earlier calculations of  $\text{TiO}_2$ -organic adsorbate interfaces [64].

To describe the presence of excess electrons in the  $\text{TiO}_2$  slabs and a positive charge (such as a dye molecule which has lost an electron) next to the  $\text{TiO}_2$  surface, a potassium atom was placed above the surface of the  $\text{TiO}_2$  (anatase or rutile) slabs. This alkaline metal is expected to donate an electron to  $\text{TiO}_2$  and form a metal cation,  $\text{K}^+$ .

Two different slab+charge models were tested – each of them for several slab thicknesses for both anatase and rutile. Model 1 (non-symmetric) has a slab with a fixed bottom layer (by "layer" we denote a  $\text{Ti}_2\text{O}_4$  repeat unit – a trilayer in rutile or 6 atomic layers in anatase) and with one K atom above the top layer. The K atom was either allowed to relax to adopt its

preferred adsorption site, or was kept fixed at a distance of 5 Å above the top surface layer. The latter configuration reflects the fact that in a typical DSSC dye molecule, after electron injection from the dye to TiO<sub>2</sub>, the dye cation's charge is localised far from the dye's adsorbing group and from the TiO<sub>2</sub> surface. Slab with thicknesses of 3 and 4 Ti<sub>2</sub>O<sub>4</sub> layers were studied. (2×3) replicated surface unit cells were used (13.12 × 8.93 Å for rutile, 11.06 × 11.46 Å for anatase). To check if the lateral dimensions are sufficient, a (3×4) replicated cell (16.59 × 15.28 Å) was also studied for a 3-layer anatase slab, and the results were very similar to the smaller (2×3) cell. This system has one unpaired electron and therefore was modelled as spin-polarised (doublet spin).

Model 2 contains a symmetric slab with two adsorbed K atoms, one above and one below the slab. All atoms are allowed to relax to find their optimum positions. With this model, we avoid the need to fix the bottom atomic layers, and larger slab thicknesses can be explored thanks to the use of symmetry in CRYSTAL. Slabs with 3, 4, 5 and 6 Ti<sub>2</sub>O<sub>4</sub> layers with (2×3) replicated surface unit cells were studied (we were not able to optimise slabs with 7 layers due to SCF convergence problems). However, the presence of two electrons donated by the two K atoms make the interpretation of the results more complicated. The two electrons can either have the same spin (triplet state) or opposite spins (singlet state); both the triplet and the singlet spin states were considered for each slab. The two models complement each other in describing large TiO<sub>2</sub> slabs.

Two sets of optimisation calculations were done. First, simple optimisation of all structures was done starting from the optimised geometries of the TiO<sub>2</sub> slabs. Then, we introduced distortions to these optimised structures, in order to encourage localisation of electrons: we selected one Ti atom in each Ti<sub>2</sub>O<sub>4</sub> layer (the atom with the largest eigenvector coefficients in each layer, according to the first set of our calculations) and distorted the structures by displacing the O atoms surrounding this Ti by 0.1 Å away from the Ti, and re-optimised the geometries. Thus, for each slab we did 2, 3 or 4 additional calculations (depending on slab thickness and symmetry). This procedure is expected to help localise the excess charge in the distorted region and is similar to the procedure used in Refs. [34] [49] [50], we additionally had a quantitative criterion for choosing the positions of distortion (Ti atoms with largest eigenvector coefficients).

These “distortion+optimisation” calculations were done for the 3-layer non-symmetric rutile slab, for 3-layer and large 4-layer non-symmetric anatase slabs, for 4-, 5- and 6-layer symmetric rutile slabs (triplet only), and all (3, 4, 5 and 6 layers) anatase slabs (all triplets and singlets). For the non-symmetric anatase and rutile slabs, the symmetric rutile slabs, and symmetric anatase slabs in the triplet state, no changes or very small changes in localisation of electron were observed compared to simple optimisation. One stable structure was obtained for each of these slabs. However, in the case of symmetric anatase slabs in the triplet spin state we obtained several distributions of excess electrons, as described in the next section.

## 2.2. Results

### 2.2.1. Geometries

After optimisation of the K on anatase structures, the K atoms were positioned approximately above the row of two-coordinated surface oxygen atoms ( $O_{2c}$ ) equidistant between two  $O_{2c}$  atoms: 1.53-1.56 Å above the layer of  $O_{2c}$ , with K- $O_{2c}$  distances of 2.53-2.56 Å. If the K atoms were kept fixed, they were positioned 5 Å above the layer of  $O_{2c}$  atoms, with K- $O_{2c}$  distances of 5.33-5.37 Å.

On rutile, K atoms after optimisation were positioned above the bond connecting 6-coordinated Ti and 3-coordinated O atoms ( $Ti_{6c}$ - $O_{3c}$  bond), with K- $Ti_{6c}$  distances of 3.23-3.28 Å, K- $O_{3c}$  distances of 2.81-2.99 Å and K- $O_{2c}$  distances of 2.57-2.62 Å to two equivalent  $O_{2c}$ . This structure is similar to the structures (labelled as the “hollow” [65] [66] [67] or “in-between” [68] site) found in earlier computational and experimental studies of K and Na on rutile (100).

### 2.2.1. Electronic properties

First, to verify that charge is indeed transferred from K to  $TiO_2$ , Mulliken charges on atoms in the  $TiO_2+K$  systems were compared to the isolated  $TiO_2$  and K. In all cases, we find that one electron has been transferred from each K atom to  $TiO_2$ . Thus, although the  $TiO_2$  slabs are defect-free (there are no oxygen vacancies or adsorbed hydroxyls), they contain excess electron charge.

Analysis of the density of states and of the highest occupied orbitals confirms that the presence of K atoms leads to the formation of defect-like states in the  $TiO_2$  band gap, similar to what is observed in systems with electron-donating dopants, oxygen vacancies or adsorbed hydroxyls [27] [28] [29] [30] [31] [32] [33] [34] [37] [38] [39] [42] [44]; these gap states are predominantly composed of Ti 3d-orbitals.

To investigate where this excess charge is localised (or delocalised) in the  $TiO_2$  slabs, spin density maps were plotted both for the systems with 1 K atom (one unpaired spin) and for the triplet systems with two K atoms (two unpaired spins).

Considering model 1 (non-symmetric slabs with 1 K), both in the three-layer and in the four-layer anatase (101) slabs spin density is distributed across several Ti atoms, with larger spin density on Ti atoms in the deeper layers (on fixed Ti atoms). Spin density for a four-layer anatase slab with a K atom 5 Å above the top layer is shown in **Figure 1** (the picture is similar both when the K atom is fixed above the surface and when K adsorbed on the surface). This tendency of the spin (and, equivalently, the excess electron) to move away from the positive charge deep into the slab and to extend laterally within the slab is different from the reported results on a single excess electron in bulk anatase and in an anatase (101) slab (negatively charged cell with compensating background positive charge) [37], where the excess electron was found to localise on one Ti atom (for a slab, on one undercoordinated Ti atom on the surface). There is better agreement with another recent study of anatase [49] which found that excess electron forms a large polaron: displacements of atoms, which were used as a measure of polaron size, were observed within the diameter of 8.6-15.2 Å from the localisation site. However, our largest (3×4) extended cell is greater than this size (16.59 ×

15.28 Å), and spin density is still delocalised along the whole length of the slab in the [010] direction (see **Figure 1**). Our results suggest that if there is a positive charge next to the anatase (101) surface then the excess negative charge in anatase is either delocalised over the whole thickness of the slab in the [010] direction or is localised in a large region, and three- and four-layer slabs are not large enough to describe this region of localisation.

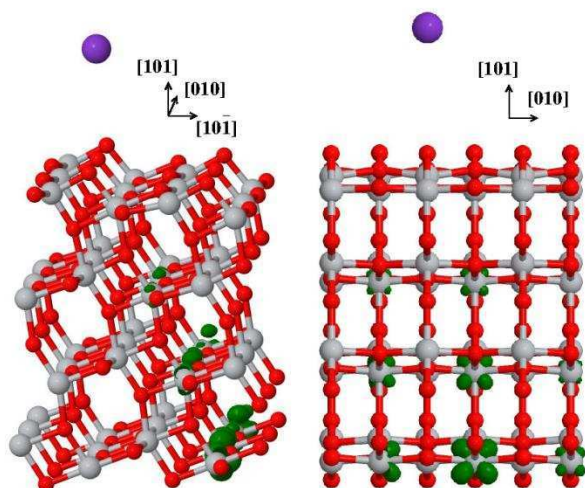


**Figure 1.** Spin density plot for a 4-layer anatase (101) slab with a K atom 5 Å above the surface (isosurface plotted in green at  $0.005 \text{ Bohr}^{-3}$ ). Spin density is delocalised over several Ti atoms in the (001) plane (perpendicular to the plane of the page in the left panel, in the plane of the page in the right panel), with larger contributions on the deeper layers which are furthest from the positively charged  $\text{K}^+$  cation.

To verify that this distribution of the charge towards the lowest layer of the slab is not caused by the lowest Ti atoms being fixed, the symmetric system (model 2) with two K atoms on the two sides of the anatase (101) slab and with no fixed atoms was analysed. Several distributions of excess electrons were obtained for each slab, depending on the distortions introduced in the system before optimisation. Structures with excess electrons predominantly distributed in the surface layer these were found to be the lowest-energy structures, followed by structures with excess electron in the subsurface layer (0.12-0.14 eV higher); a structure with excess electron the second subsurface layer was also found in the 5-layer slab and was 0.33 eV above the minimum. **Figure 2** shows the spin density distribution for the lowest-energy structure of the six-layer symmetric slab. Spin is delocalised over several surface 6-coordinated Ti atoms, with the largest contributions on one Ti atom at each surface; there are also contributions from atoms in the subsurface layer. Thus, excess electron is spread across the width of our slab (3 repeat units) in the [010] direction. These results are different from the behavior of non-symmetric slabs. Since non-symmetric slabs contain fixed atoms, these may create artificial low-energy states, therefore we proceed with symmetric slabs which do not contain any fixed atoms. The calculated spin distribution in the symmetric anatase slabs is similar to that reported in Ref. [47] for the surface oxygen vacancy in anatase, where excess electron are distributed over several surface and subsurface Ti atoms, predominantly those near the vacancy.



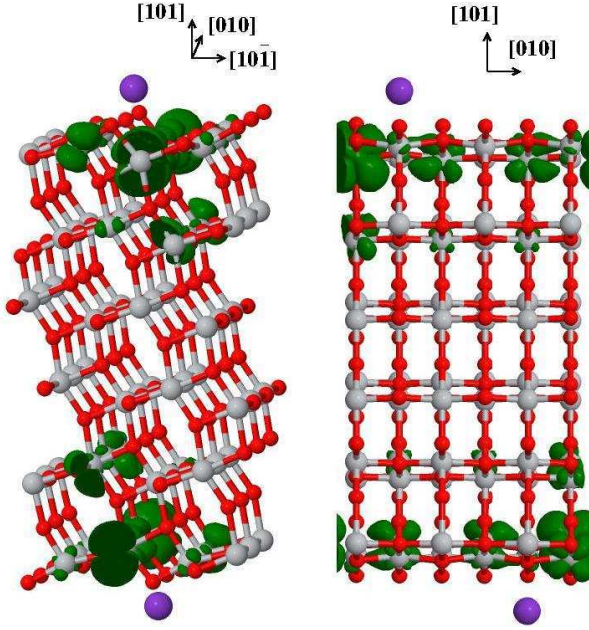


**Figure 2.** Spin density plot for a 6-layer symmetric anatase (101) slab with two K atoms adsorbed at the surfaces (isosurface plotted in green at  $0.0005 \text{ Bohr}^{-3}$ ). Spin density is spread over several Ti atoms, especially surface ones.

The two excess electrons in model 2 can also have opposite spins and reside in the same orbital. For the closed-shell systems, it is not possible to plot spin density, but the distribution of coefficients of the highest occupied orbitals shows that these orbitals are spread over many Ti atoms. However, this singlet state was found to be less stable than the triplet by 0.4-0.5 eV in anatase and by 0.8-1.1 eV in rutile.

To quantify the spatial distribution of excess electron across the slab, we calculated inverse participation ratio (IPR)  $P_i$  for each of the systems. IPR is a way of quantifying localisation or delocalisation of a state [69]. It can be expressed for non-orthonormal basis functions as [69] [70]:

$$P_i = \frac{\sum_r |\psi_i(r)|^4}{\left| \sum_r (\psi_i(r))^2 \right|^2} \quad (1)$$

where  $\psi_i(r)$  is a single-particle wavefunction for the orbital  $i$  occupied by the additional electron, and  $r$  are lattice sites. In the limiting case of the wavefunction spread equally over all available sites,  $P_i$  tends to zero. If the wavefunction is spread equally over  $L$  lattice sites (out of possible  $N$  sites) with equal amplitude then  $P_i = 1/L$ . In the other limiting case of the wavefunction localised on one orbital,  $P_i = 1$  [69].

In the hypothetical case where the excess electron is fully delocalised over all Ti and O atoms of a slab, IPR (calculated as  $1/N$  where  $N$  is the number of atoms) would be between 0.004 and 0.014 (or 0.01-0.04 if only Ti atoms are considered) for the system sizes used in our study.

In our non-symmetric slabs the values of IPR calculated according to equation (1) range from 0.19 (three-layer slab) to 0.04 (four-layer), and in symmetric slabs from 0.17 (three-layer) to 0.27 (five- and six-layer) for triplet states or only from 0.04 to 0.02 for singlet states. These values are larger than a fully delocalised solution, but show that the excess electron is not fully localised. The IPR values for different-size slabs, together with the spin plot (**Figures 1 and 2**) show that the vertical extension of the largest (5- and 6-layer) slabs is sufficient to accommodate the excess electron density, but the lateral extension of the slab (3 repeat units) is not sufficient.

To visualise this electron distribution, we analysed the wavefunction coefficients ( $c_{ij}$ ) for the orbitals ( $j$ ) occupied by excess electrons. For each layer ( $l$ ) of the slab, the sum of squares of wavefunction coefficients for atoms belonging to this layer was calculated as  $s(l) = \sum_j \sum_{i=1}^{n(l)} c_{ij}^2$ , where  $n(l)$  is the number of basis functions on atoms in each particular layer  $l$  and  $j$  is the HOMO (singlet state) or the two SOMOs (triplet state). Then, the fractions of these orbitals on each layer were calculated:

$$f(l) = \frac{s(l)}{|\psi|^2} = \frac{\sum_j \sum_{i=1}^{n(l)} c_{ij}^2}{\sum_j \sum_{i=1}^N c_{ij}^2} \quad (2)$$

where  $N$  is the total number of basis functions and  $\psi$  is the wavefunction of the HOMO or the SOMO.

These fractions, i.e. contributions of each layer to the orbitals occupied by excess electrons, are shown in **Figure 3**. The figure describes the most stable structures for each slab thickness; metastable structures are additionally included only for the 5-layer symmetric slab. The graphs in **Figure 3** confirm that the singly occupied orbitals in rutile slabs have the largest weight on the first subsurface layer. Anatase slabs behave in different ways depending on their symmetry and size: in non-symmetric anatase slabs these orbitals have the largest weight on deeper layers away from the counterion (top left graph); in symmetric anatase slabs with 4 and more layers these orbitals are located predominantly on the primarily surface layers (top right graph). The metastable electron arrangements in anatase have the SOMOs primarily distributed over subsurface Ti (structure 0.12 eV above the most stable one) and into the second subsurface layer (structure 0.33 eV above the most stable one).

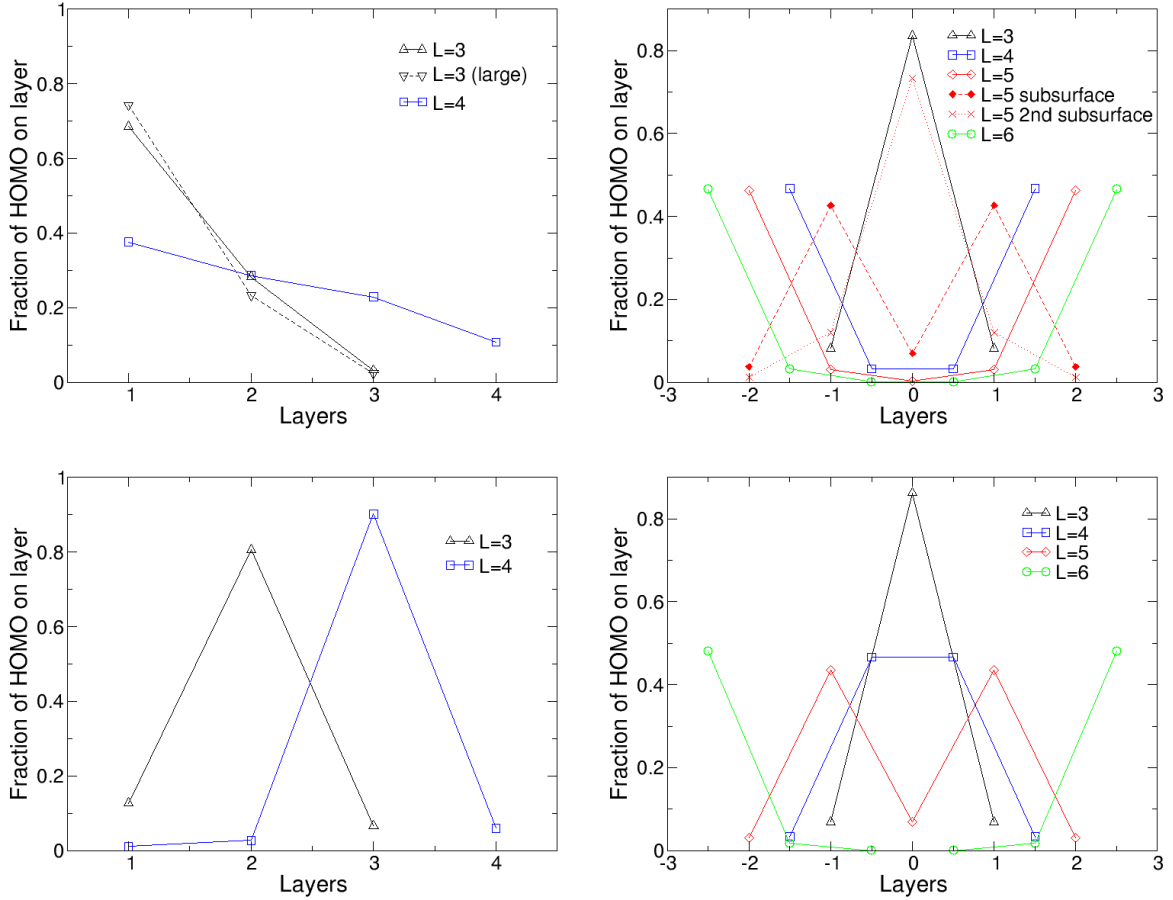


**Figure 3.** Contribution of each layer in the  $\text{TiO}_2$  slab to the orbitals which house excess electrons. Upper panels: anatase slabs; lower panels: rutile slabs; left panels: non-symmetric slabs (model 1), right panels: symmetric slabs (model 2). Only the lowest-energy structures are plotted for symmetric anatase slabs; metastable structures are included for illustration for one case of the 5-layer anatase slab. For rutile symmetric slabs, each slab has only one stable electron arrangement; singlet structures (not shown) look very similar to triplets. Black lines and triangles: three-layer slabs; blue lines and squares: four-layer slabs; red lines and diamonds: five-layer slabs; green lines and circles: six-layer slabs. In all the plots, the layers labelled with the largest number are the outer layers, next to adsorbed potassium ions.

The situation is somewhat different in rutile (110) slabs: spin is more strongly localised. In the symmetric slabs (singlet and triplet state) spin is distributed over several Ti atoms, mainly in the first subsurface layer (on Ti atoms below surface  $\text{Ti}_{5c}$  atoms), with one atom in the subsurface layer having the largest contribution (or, equivalently, two atoms in two subsurface layers for the symmetric systems with two excess electrons), see **Figure 4**. The 6-layer rutile slab is an exception, with the excess electron residing in the surface layer, despite several optimization runs (see orbitals' spatial distributions in **Figure 3**). This distribution of electrons is similar to the widely studied oxygen vacancy in rutile (110), where localisation of the two excess electrons is even stronger (the two excess electrons are entirely localised on two subsurface Ti atoms) [31] [33] [34] [47] [50]. In the non-symmetric slabs (3 or 4  $\text{Ti}_2\text{O}_4$  trilayers with fixed bottom trilayer), the spin is strongly localised on one atom and to a

smaller extent on a second Ti atom in the first subsurface layer, again very similar to the oxygen vacancy in rutile (110) vacancies [31] [33] [47] [50].

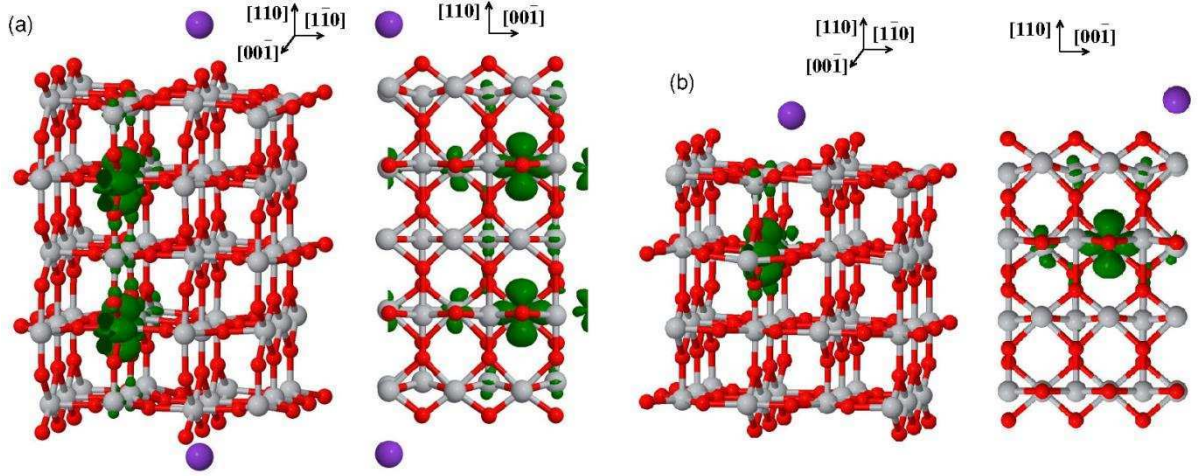


**Figure 4.** Spin density plots: (a) for a 5-layer symmetric rutile (110) slab with two K atoms adsorbed at the surfaces, (b) for a 4-layer non-symmetric rutile(110) slab with one K atom adsorbed (isosurfaces plotted at  $0.0025 \text{ Bohr}^{-3}$ ). Spin density is distributed over several Ti atoms, with the principal contributions of one Ti atom in the first subsurface layer.

IPR values calculated for rutile slabs are between 0.16 and 0.33 for symmetric slabs in the triplet state (0.16-0.04 for singlet states), similar but slightly higher than the values for anatase slabs, showing that excess electron is somewhat delocalised; they rise to 0.35-0.52 for non-symmetric rutile slabs, indicating stronger localisation. These values are in agreement with the fractions of the SOMO on each of the layers shown in **Figure 3**: localisation is slightly stronger in rutile than in anatase slabs, especially in the non-symmetric rutile slabs; there are large contributions from several atoms in the first subsurface layer and much smaller contributions of the deeper layers.

In summary, DFT calculations show that the excess electron is delocalised over multiple Ti sites. Especially in anatase, excess electron can be described as delocalised laterally in a large region along the [010] direction, larger than system sizes accessible to DFT calculations (slabs with up to  $16.6 \times 15.3 \text{ \AA}$  lateral dimensions). Alternative methods capable of treating large system sizes, such as continuum methods, are needed for proper description of excess electron in  $\text{TiO}_2$ .

### 3. Continuum model of excess electron in $\text{TiO}_2$

#### 3.1. Description of the model

An effective one body Hamiltonian for the excess electron in the CB is now considered, to reduce the number of degrees of freedom. This Hamiltonian is applicable when the electronic wavefunction is delocalised over a large spatial region in comparison to the crystal unit cell,

as also required by the effective mass approximation employed. The presence of an interface between the nanocrystal and the electrolyte is described using the image charge formalism [71] [72] [73] [74]. In cylindrical coordinates  $\mathbf{r}=(\rho, \varphi, z)$ , this can be expressed as [75]:

$$\hat{H} = -\frac{\hbar^2}{2\mu} \nabla_{\mathbf{r}}^2 - \frac{\beta e^2}{16\pi\epsilon_0\epsilon_2 z} - \frac{\gamma e^2}{4\pi\epsilon_0 \sqrt{\rho^2 + (z+z_h)^2}} \quad (3)$$

where the constants introduced are the reduced Plank's constant  $\hbar$ , the electron effective mass  $\mu$ , the elementary charge  $e$ , the vacuum permittivity  $\epsilon_0$ , the macroscopic dielectric constant for the two media, respectively:  $\epsilon_1$  (for the electrolyte solution) and  $\epsilon_2$  (for the semiconductor). The positive charge embedded in the first medium has been positioned at  $(0, 0, -z_h)$ , as shown by the sketch **Figure 5**.

The potential energy term in the Hamiltonian above comprises of two contributions, each of them with a distinctive symmetry. The first term is due to the image charge generated by the electron at the interface and depends on the coordinate along the  $z$ -axis orthogonal to the surface of the semiconductor, while the last term takes into account the Coulomb contribution arising from the positive point charge at  $-z_h$  and is spherically symmetrical. The constants  $\beta$  and  $\gamma$  are related to the dielectric constants through [75]:  $\beta = (\epsilon_2 - \epsilon_1)/(\epsilon_2 + \epsilon_1)$  and  $\gamma = 2/(\epsilon_2 + \epsilon_1)$ .

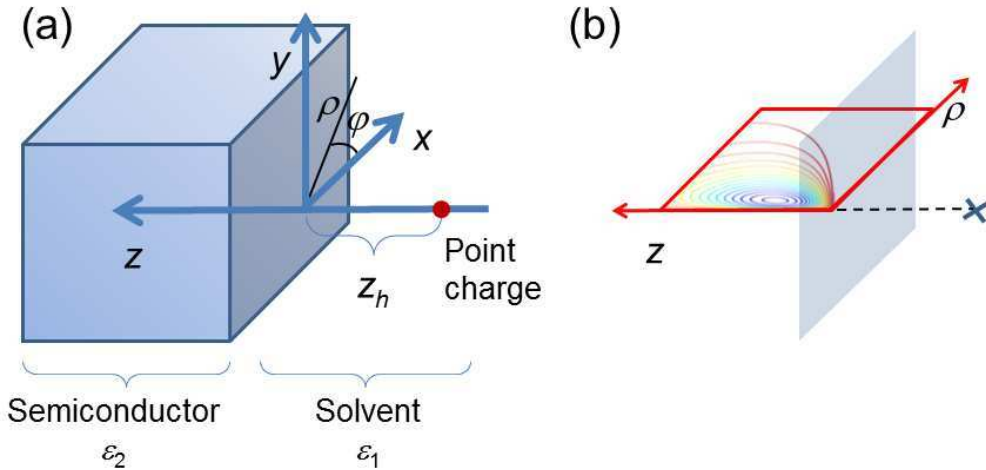


**Figure 5.** (a) Sketch of the model system and cylindrical coordinate system employed. (b) Section plane (highlighted in red) in which the electronic wavefunction will be evaluated. The plane is orthogonal to the interface between the two media (in grey) and contains the point-like charge. Illustrative contour plot for the electron wavefunction is also shown in the section plane.

The potential energy operator does not depend on the coordinate  $\varphi$ , hence eigenfunctions of the operator  $\hat{1}_z = -i\hbar \frac{\partial}{\partial \varphi}$  will factorise from the overall solution, leading to a dependence on

the angular quantum number  $m$ . We will label the solutions obtained for different values of  $m$  following the practice for systems with spherical symmetry:  $m = 0 \rightarrow s$ ,  $m = \pm 1 \rightarrow p$  and so on. An approximate solution is found using the linear variational technique. A suitable basis set for the radial coordinate is given by the Landau states [72] [76]:

$$R_l^{(m)}(\xi) = \sqrt{\sigma} \frac{1!}{\sqrt{(1+|m|)!}} e^{-\frac{\xi}{2}} \xi^{\frac{|m|}{2}} L_1^{(m)}(\xi) \quad (4)$$

where with  $L_1^{(m)}(\xi)$  we have indicated the generalised Laguerre polynomials defined as a function of the scaled variable  $\xi = \frac{\sigma}{2} \rho^2$ , of the principal quantum number  $l = 0, 1, 2, \dots$  and of the angular quantum number  $m = 0, \pm 1, \pm 2, \dots$ . For the  $z$  coordinate we employ the eigenfunctions of the particle in a box:

$$\Lambda_v(z) = \sqrt{\frac{2}{L}} \sin\left(\frac{v\pi}{L} z\right) \quad (5)$$

with  $L$  we indicate one endpoint of the domain  $[0, L]$  on which the basis set is defined; this definition of the domain is consistent with the boundary condition  $z > 0$  which we assumed on a physical basis. The quantum number  $v$  takes non-negative integer values. We refer to the appendix for the explicit evaluation of the Hamiltonian matrix elements. The variational wavefunction can be expressed as a linear combination of the basis set elements:  $\Psi(\xi, z) = \sum_{l,v} C_{l,v} R_l^{(m)}(\xi) \Lambda_v(z)$ . The parameters defining the basis set  $L$  and  $\sigma$  have been

defined as those minimizing of the lowest eigenvalue [77] for a given basis set size via a BFGS search algorithm [78].

### 3.2. Choice of the model parameters

To completely specify the model, other quantities are required: these are the dielectric constants for the two media and the effective electron mass. There is a large amount of uncertainty concerning the value of electron effective mass in  $\text{TiO}_2$  obtained experimentally (typically, they are obtained from the analysis of Hall coefficients, conductivity and thermoelectric power): values for rutile have been reported in the range between  $5 m_e$  and  $13 m_e$  [79] [80] [81] [82] and as large as  $12$ - $32 m_e$  [83]; however, it has been argued that the measured value is the mass of a polaron, while the mass of a bare electron is smaller, of the order of  $3 m_e$  [80] or  $6$ - $7 m_e$  [84]. For anatase nanoparticles, the measured values are much smaller,  $\sim 1 m_e$  [85] or  $0.71$ - $1.26 m_e$  [86] depending on particle size. DFT calculations show that electron effective mass in both rutile and anatase is strongly anisotropic, between  $0.6$ - $1.2 m_e$  for rutile [87] [88] and  $0.04$ - $0.48$  for anatase [88]; optical effective mass which takes into account all occupied states in the conduction band has been calculated as  $\sim 0.5 m_e$  and  $\sim 4 m_e$  (direction-dependent) for anatase [89]. We find, by numerical differentiation of the lowest CB level near the  $\Gamma$  point, the values of  $2.1 m_e$  and  $1.1 m_e$  for the  $\Gamma X$  and  $\Gamma Z$  directions in

bulk rutile and  $0.9 m_e$  and  $0.8 m_e$ , respectively, in bulk anatase. However, for the model we adopt the values based on experiment:  $1.22 m_e$  consistent with anatase [86] and  $10 m_e$  consistent with rutile [79] [81] [82] and we will discuss the effect of changing the effective mass on the electron localisation.

The dielectric constant of  $\text{TiO}_2$  ( $\epsilon_2$ ) is also ambiguous: in crystalline rutile, it is large and anisotropic (170 in the  $c$  direction and 86 in the  $a$  direction at room temperature, in units of vacuum permittivity) [90], while in anatase the measured values vary strongly (from  $\sim 10$  to  $\sim 70$ ) depending on film thickness, method of preparation and frequency of the applied electric field [91] [92]: e.g. in 90-105 nm films the dielectric constant was measured as 13-18 [91], the value of  $12 \pm 4$  was suggested for anatase films consisting of  $8.0 \pm 0.2$  nm particles [82]; the latter value is used in this model. This parameter is also varied in our study, to study its effect on electron localisation.

The dielectric constant for bulk acetonitrile ( $\epsilon_1$ ) is non-ambiguously reported as 36.6 [93]. The presence of a solid interface, however, is known to affect the value of the dielectric constant for electrolytic solutions and it can be determined by solving the Poisson-Boltzmann equation for a given solute concentration. We will not pursue this approach here as it is not congruous with our theoretical framework and it would not be conclusive for the model presented as there are uncertainties on other parameters; we therefore assume that the behaviour shown by aqueous solutions in ref. [94] can be extended to the case of acetonitrile and take the value of  $\epsilon_1$  to be one tenth of the value in bulk, i.e.  $\epsilon_1 = 3.66$ . This approach is consistent with the aim of this study, which is to provide a conservative estimate of the exciton radius. Indeed, for big values of  $\epsilon_1$  (or, alternatively, small values of  $\epsilon_2$ ) the electron is more delocalised as the image charge interaction that binds it to the interface becomes repulsive for  $\epsilon_1 > \epsilon_2$  and the attractive Coulomb term in equation (3) is screened by the prefactor  $\gamma$ .

### 3.3. Results

To describe the excess electron at the  $\text{TiO}_2$ /electrolyte interface, we solve the Hamiltonian in equation (3) for the values of dielectric constants corresponding to the  $\text{TiO}_2$  and electrolyte phases. **Figure 6** visualises the first six states at the lowest energies: we report the contour plots for a section of the wavefunction in the plane  $\varphi = 0$  (shown in red in **Figure 5b**). The states are labelled as 1s, 1p, 2s, 1d, 2p, 3s, according to the values of their principal quantum number  $l$  and angular quantum number  $m$  (cf. equation (4)), with the conventional notation  $m=0 \rightarrow s$ ,  $|m|=1 \rightarrow p$ ,  $|m|=2 \rightarrow d$ . The plots in **Figure 6** are obtained for a value of electron effective mass  $\mu = 10 m_e$ , and the dielectric constants values introduced in the previous section:  $\epsilon_1 = 3.66$ ,  $\epsilon_2 = 12$ ; the positive charge has been positioned at  $2.4 \text{ \AA}$  from the interface, this value is compatible with the adsorption distance of an alkaline metal ion on the anatase (101) surface.



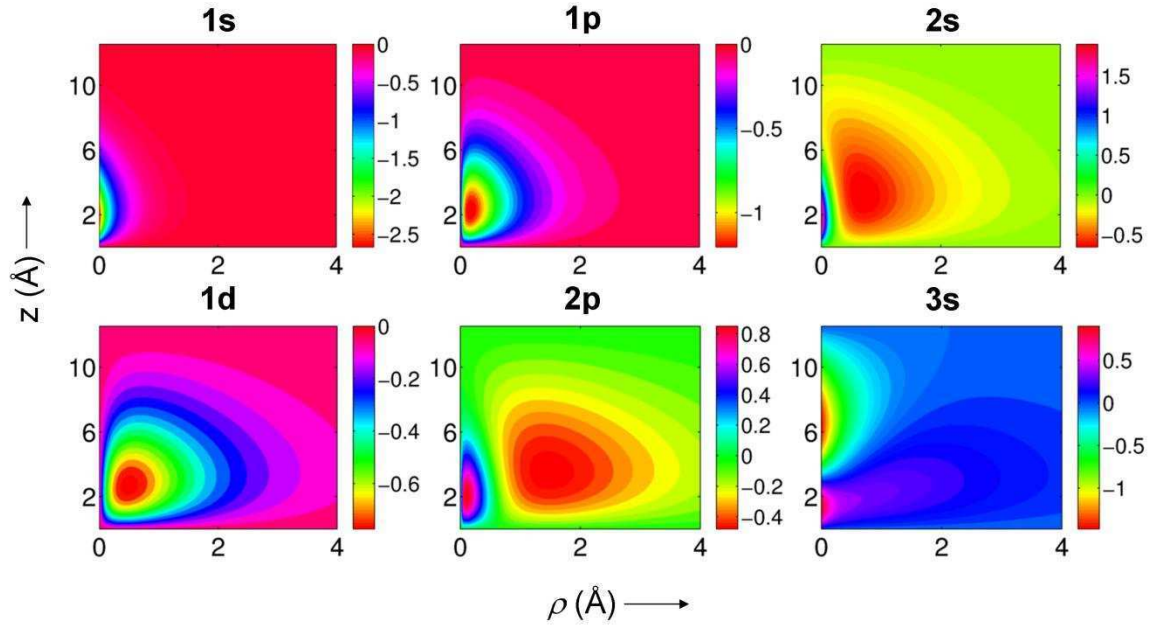


**Figure 6.** Contour plot for the electronic wavefunction, their respective energies are  $E(1s) = -0.27$  eV,  $E(1p) = -0.19$  eV,  $E(2s) = -0.16$  eV,  $E(1d) = -0.15$  eV,  $E(2p) = -0.13$  eV,  $E(3s) = -0.13$  eV. States are labelled according to the values of the principal and angular quantum numbers ( $l, m$ ). Model parameters set as  $z_h = 2.4$  Å,  $\epsilon_1 = 3.66$ ,  $\epsilon_2 = 12$ ,  $\mu = 10 m_e$ .

The impact of the effective electron mass and of the semiconductor's dielectric constant, i.e. the two parameters affected by bigger experimental uncertainties, on the exciton ground state energy is analysed in **Figure 7**. The average value for the exponential trap distribution has been identified experimentally within  $-0.09$  eV and  $-0.14$  eV (with the energy zero being the  $\text{TiO}_2$  conduction band edge) and it is marked in **Figure 7** by dashed lines. Interestingly, different intervals of  $\epsilon_2$  are compatible with the observed shallow trap energy for different values of the effective mass, in particular for  $\mu = 1.22 m_e$  the permissible range for  $\epsilon_2$  overlaps with the experimental estimate of  $12 \pm 4$  reported for anatase in Ref. [82]. For heavier values of the electron mass more closely corresponding to rutile (shown in the right panel of **Figure 7**) the ground state is far lower in energy and for values of  $\epsilon_2$  near 10 gives a trap state positioned  $\sim 0.3$  eV below the conduction band edge; larger values of  $\epsilon_2 = 20-30$  (though smaller than  $\epsilon_2$  measured for bulk rutile [90]) are needed to give shallow trap states. In any case these states are not as deep as those associated with oxygen vacancies (with trapping energy over 0.5 eV) [31] [35] [95].



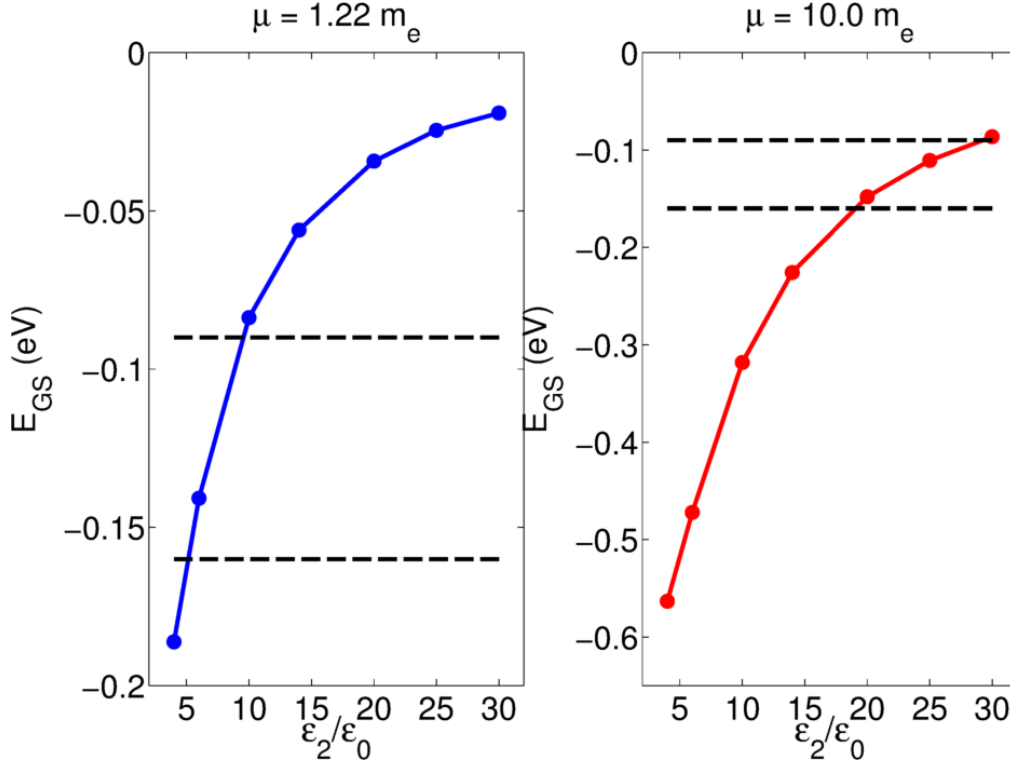


**Figure 7.** Ground state energy for the exciton obtained for  $z_n = 2.43 \text{ \AA}$  and  $\epsilon_1 = 3.66$  as a function of the other model parameters. Dashed lines represent average values for exponential trap distributions as found in two different experimental studies, Ref. [20] (0.16 eV below the CB minimum) and Ref. [3] (0.09 eV below the CB minimum) .

We now evaluate the ground state exciton localisation for the two values of  $\mu$  considered, while keeping  $\epsilon_2$  in the permissible physical range. To better quantify the localisation of the electron, we define the exciton radius as the expectation value of the cubic root of the ‘volume’ operator  $\hat{\rho}^2 \hat{z}$ :

$$R = \langle \Psi_{1s} | \sqrt[3]{\rho^2 z} | \Psi_{1s} \rangle \quad (6)$$

where the subscript 1s identifies the ground state wavefunction; the values of  $R$  are reported in **Table 1** together with the expectation values for the spatial coordinates and their uncertainties. In both cases considered here, the exciton radius is far bigger than the elementary cell of  $\text{TiO}_2$  anatase, in agreement with what is found from DFT simulations of the interface.

In the calculations for the rutile-like system (large dielectric constant and electron effective mass, right column of **Table 1**), the depth ( $z$  value) of the exciton is smaller than for anatase; the lateral extension of the exciton ( $\rho$ ) is also smaller than for anatase, but in both cases it is still much larger than the primitive cell and the size of the cell in our DFT computations.

**Table 1.** Exciton radius (expectation value and variance) for selected values of the semiconductor dielectric constant and electron effective mass.  $z_0 = 2.4 \text{ \AA}$  and  $\epsilon_1 = 3.66$ . Values in Ångströms.

$\mu = 1.22 m_e$				$\mu = 10.0 m_e$			
$\epsilon_2$	R	$\langle \rho \rangle \pm \delta \rho$	$\langle z \rangle \pm \delta z$	$\epsilon_2$	R	$\langle \rho \rangle \pm \delta \rho$	$\langle z \rangle \pm \delta z$
6	174.8	$453 \pm 240$	$29.3 \pm 4.7$	20	47.85	$93.4 \pm 49.3$	$14.0 \pm 2.0$
10	218.2	$586 \pm 310$	$34.0 \pm 5.3$	25	41.94	$78.1 \pm 41.2$	$13.7 \pm 2.3$
14	513.0	$1930 \pm 1020$	$42 \pm 13$	30	41.92	$120 \pm 63$	$6.2 \pm 3.3$

## 4. Conclusions

Two different models of the photoinjected electron in the semiconductor's conduction band in the presence of a positive charge at fixed distance from the semiconductor surface have been presented. Atomistic (DFT) calculations show that the excess electron is either delocalised in  $\text{TiO}_2$  or is localised in a large region, with lateral dimensions larger than system sizes accessible to DFT calculations. An alternative model, based on a one-electron effective Hamiltonian, has been used to treat large system sizes. This model is able to reproduce, for a reasonable choice of the system's parameters, the binding energies observed experimentally for shallow trap states in  $\text{TiO}_2$  in DSSCs, hence supporting an experimental conjecture [10] of excess electron-cation interaction as the origin of these shallow trap states. The electron delocalisation has been evaluated for these physically justified values of the parameters and the value of the exciton radius is comparable with the size of the  $\text{TiO}_2$  nanoparticles used to assemble the photoanode.

Several experimental studies [10] [12] [11] [23] [24] indicate the presence of shallow trap states in anatase nanoparticles. However, the nature of these states is not yet clear, as discussed in the Introduction. Both localised and delocalised nature of these states has been inferred from experiments [11] [23] [24] [25] [26]. We suggest, based on our study, that electrons donated by ionizable adsorbates (metal ions in this model study, and possibly also electron-injecting dyes in dye-sensitised solar cells) are responsible for these shallow trap states.

In this model we have selected the parameters based on the available experimental evidence. Under many circumstances, such as for  $\epsilon_1$  values comparable with its solution bulk value or for oxidised dyes of bigger size (with the positive charge density located further

from the interface), the exciton binding energy can become smaller than the thermal energy and the existence of these states can be neglected when describing the initial state of the charge recombination process.

A limitation of the model presented lies in the minimal description of the molecular system adsorbed on the semiconductor's surface. This limitation restricts the applicability of the model, in particular since recent experimental studies have shown that depending on the molecular species adsorbed the charge transfer exciton was localised near the interface or delocalised over the whole nanoparticle [96]. To provide a complete ab initio description of the system it would be necessary to move beyond the mean field level of theory and explicitly account for many-body effects. The theoretical framework in this instance is provided by the Bethe-Salpeter equation, which includes not only the direct coulomb interaction between electron and hole forming the exciton, but also the exchange interaction screened by the presence of other electrons [97]. Given the high computational demands of this method, it is not surprising that to date it has only been applied to bulk solids. However, in the case of organic molecules crystals the solution of the Bethe-Salpeter equation was able to shed light on the nature of the charge transfer states and to relate it to the underlying electronic structure of these materials [98]. We believe that the application of many-body techniques should prove very beneficial to the study of charge transfer in heterogeneous systems, such as those mentioned in the introduction of this study, as a benchmark of effective one body models.

This paper highlights one of the main problems in modelling photoinduced charge transfer processes at the interface between an inorganic material and a molecule. The elementary processes involve states with different degrees of localisation which are normally modelled with different degrees of accuracy. The excited molecular state that initiates the charge injection process and the molecular HOMO that is the final one-electron state after charge recombination are well described by electronic structure method. The injected electron displays a degree of delocalisation, where an effective one-electron model may be more accurate than an atomistic DFT calculation. The ability to combine different descriptions to study charge transfer processes rather than just the initial and final states is one of the main challenges in this field.

## 5. Appendix A

Here we report the explicit derivation for the Hamiltonian matrix elements evaluated over the basis set functions. We report the Hamiltonian as a starting point:

$$\hat{H} = -\frac{\hbar^2}{2\mu} \nabla_{\mathbf{r}}^2 - \frac{\beta e^2}{16\pi\epsilon_0\epsilon_2 z} - \frac{\gamma e^2}{4\pi\epsilon_0 \sqrt{\rho^2 + (z+z_h)^2}} \quad (\text{A.1})$$

where the symbols have been defined in Section 3 of the main text. Since the potential energy term does not depend on the angular coordinate, it is possible to factorise out the solution as  $\Omega(\rho, \varphi, z) = \chi(\rho, z) \cdot \Phi(\varphi)$ , and therefore the eigenvalue equation can be recast as:

$$\begin{cases} -\frac{\hbar^2}{2\mu} \left\{ \frac{\partial^2}{\partial \rho^2} + \frac{1}{\rho} \frac{\partial}{\partial \rho} - \frac{m^2}{\rho^2} + \frac{\partial^2}{\partial z^2} \right\} \chi(\rho, z) - \frac{e^2}{4\pi\epsilon_0} \left\{ \frac{\beta}{4\epsilon_2 z} + \frac{\gamma}{\sqrt{\rho^2 + (z+z_h)^2}} \right\} \chi(\rho, z) = E\chi(\rho, z) \\ \frac{d^2}{d\varphi^2} \Phi(\varphi) = -m^2 \Phi(\varphi) \end{cases} \quad (\text{A.2})$$

This allows us to immediately find the angular dependence in the effective one body wavefunction as:  $\Phi(\varphi) = \frac{1}{\sqrt{2\pi}} e^{im\varphi}$ ; in order to meet periodicity requirement we must have  $m=0, \pm 1, \pm 2, \dots$ . The original problem has been reduced to two dimensions, depending on the additional parameter  $m$  which is can be thought of as an angular quantum number [99].

To address the variational solution for the model above, we perform a change of variable for the radial coordinate:  $\xi = \frac{\sigma}{2} \rho^2$  where  $\sigma$  is a scaling coefficient which can be obtained by variational minimisation of the ground state energy. The top equation in (A.2) reads:

$$-\frac{\hbar^2}{2\mu} \left\{ 2\sigma\xi \frac{\partial^2}{\partial \xi^2} + 2\sigma \frac{\partial}{\partial \xi} - \frac{\sigma m^2}{2\xi} + \frac{\partial^2}{\partial z^2} \right\} \psi(\xi, z) - \frac{e^2}{4\pi\epsilon_0} \left\{ \frac{\beta}{4z} + \frac{\gamma}{\sqrt{\frac{2}{\sigma}\xi + (z+z_h)^2}} \right\} \psi(\xi, z) = E\psi(\xi, z) \quad (\text{A.3})$$

This equation can be solved approximately using the variational method. We proceed with the evaluation of the terms containing differential operators. This is written as

$$\hat{D}_T = -\frac{\hbar^2}{2\mu} \left\{ \frac{1}{\rho} \frac{\partial}{\partial \rho} \left( \rho \frac{\partial}{\partial \rho} \right) + \frac{\partial^2}{\partial z^2} \right\} \quad (\text{A.4})$$

Hence the kinetic part of the Hamiltonian matrix can be evaluated through the integral:

$\langle \mathbf{R}_k^{[m]} \Lambda_w | \hat{K}_T | \mathbf{R}_l^{[m]} \Lambda_v \rangle$ , with  $\hat{K}_T = \hat{D}_T + \frac{\hbar^2 m^2}{\mu \rho^2}$ . This can, in turn, be decomposed according to:

$$\langle \mathbf{R}_k^{[m]} \Lambda_w | \hat{K}_T | \mathbf{R}_l^{[m]} \Lambda_v \rangle = \langle \mathbf{R}_k^{[m]} | \hat{K}_\xi | \mathbf{R}_l^{[m]} \rangle \cdot \langle \Lambda_w | \Lambda_v \rangle + \langle \mathbf{R}_k^{[m]} | \mathbf{R}_l^{[m]} \rangle \cdot \langle \Lambda_w | \hat{K}_z | \Lambda_v \rangle \quad (\text{A.5})$$

The matrix elements for the  $z$  part are particularly straightforward to evaluate:

$$\langle \Lambda_w | \hat{K}_z | \Lambda_v \rangle = \frac{\hbar^2}{2\mu} \cdot \frac{2}{L} \cdot \frac{v^2 \pi^2}{L^2} \int_0^L dz \sin\left(\frac{w\pi}{L} z\right) \sin\left(\frac{v\pi}{L} z\right) \quad (\text{A.6})$$

For the radial coordinate the integral is more involved because of the change of variable to carry out both in the differential operator and in the integral. We give therefore an explicit account for the expression to compute (with  $m$  we refer to the absolute value of the angular quantum number) for the integrals:

$$\left\langle \mathbf{R}_k^m \left| -\frac{d^2}{d\rho^2} \mathbf{R}_l^m \right. \right\rangle = -\left\langle \mathbf{R}_k^m \left| \left( \frac{d\xi}{d\rho} \right)^2 \frac{d^2}{d\xi^2} + \frac{d^2\xi}{d\rho^2} \frac{d}{d\xi} \mathbf{R}_l^m \right. \right\rangle \quad (\text{A.7})$$

$$\left\langle \mathbf{R}_k^m \left| -\frac{1}{\rho} \frac{d}{d\rho} \mathbf{R}_l^m \right. \right\rangle = -\left\langle \mathbf{R}_k^m \left| \sqrt{\frac{\sigma}{2\xi}} \frac{d\xi}{d\rho} \frac{d}{d\xi} \mathbf{R}_l^m \right. \right\rangle \quad (\text{A.8})$$

Rearranging the previous integrals we can define two distinct contributions to the kinetic term  $\langle \mathbf{R}_k^m | \hat{\mathbf{K}}_\xi | \mathbf{R}_l^m \rangle = N_{k,l} \{ \mathbf{T}_{k,l} + \mathbf{K}_{k,l} \}$ , where:

$$\mathbf{T}_{kl} = -\int_0^{+\infty} d\xi e^{-\frac{\xi}{2}} \xi^{\frac{m}{2}} L_k^m(\xi) \left( 2\xi \frac{d^2}{d\xi^2} \left( e^{-\frac{\xi}{2}} \xi^{\frac{m}{2}} L_l^m(\xi) \right) \right) \quad (\text{A.9})$$

$$\mathbf{K}_{kl} = -\int_0^{+\infty} d\xi e^{-\frac{\xi}{2}} \xi^{\frac{m}{2}} L_k^m(\xi) \left( 2 \frac{d}{d\xi} \left( e^{-\frac{\xi}{2}} \xi^{\frac{m}{2}} L_l^m(\xi) \right) \right) \quad (\text{A.10})$$

The final expression, combining the previous two, reads:

$$\langle \mathbf{R}_k^m | \hat{\mathbf{K}}_\xi | \mathbf{R}_l^m \rangle = N_{kl} \left\{ \left( 1 + \frac{m}{2} + \frac{1}{2} \right) I[m, k, l] - \frac{m^2}{4} I[m-1, k, l] - \frac{1}{4} I[m+1, k, l] \right\} \quad (\text{A.11})$$

where we have used the shorthand notation:  $I[m+\alpha, i, j] = \int_0^{+\infty} d\xi e^{-\xi} \xi^{m+\alpha} L_i^m(\xi) L_j^m(\xi)$  and  $N$  is the normalisation constant.

The potential term is more obvious and can be obtained immediately as the sum of two contributions:

$$\langle \mathbf{R}_k^m \Lambda_w | \hat{\mathbf{V}}_T | \mathbf{R}_l^m \Lambda_v \rangle = \langle \mathbf{R}_k^m | \mathbf{R}_l^m \rangle \cdot \langle \Lambda_w | \hat{\mathbf{V}}_\beta | \Lambda_v \rangle + \langle \mathbf{R}_k^m \Lambda_w | \hat{\mathbf{V}}_\gamma | \mathbf{R}_l^m \Lambda_v \rangle \quad (\text{A.12})$$

Where we have implicitly defined the operators:  $\hat{\mathbf{V}}_\beta = \frac{e^2}{4\pi\epsilon_0} \cdot \frac{\beta}{4\epsilon_2 \hat{z}}$  and  $\hat{\mathbf{V}}_\gamma = -\frac{e^2}{4\pi\epsilon_0} \cdot \frac{\gamma}{\sqrt{2\sigma\xi + \sigma^2} (\hat{z} + z_h)^2}$ , where we indicate the position operators with the corresponding spatial variables with a hat sign. The abstract notation above can be recast in terms of its real space representation as:

$$\langle \Lambda_w | \hat{\mathbf{V}}_\beta | \Lambda_v \rangle = -\frac{e^2 \beta}{16\pi\epsilon_0 \epsilon_2} \frac{2}{L} \int_0^L dz \sin\left(\frac{w\pi}{L} z\right) \frac{1}{z} \sin\left(\frac{v\pi}{L} z\right) \quad (\text{A.13})$$

$$\langle \mathbf{R}_k^m \Lambda_w | \hat{\mathbf{V}}_\gamma | \mathbf{R}_l^m \Lambda_v \rangle = -\frac{e^2 \gamma}{4\pi\epsilon_0} \cdot \frac{2}{L} N_{k,l} \iint_D d\xi dz \sin\left(\frac{w\pi}{L} z\right) e^{-\xi} \xi^m L_k^m(\xi) \frac{1}{\sqrt{2\sigma\xi + \sigma^2} (z + z_h)^2} \sin\left(\frac{v\pi}{L} z\right) L_l^m(\xi) \quad (\text{A.14})$$

In the previous equation the integration domain  $D$  stands for  $[0, \infty) \times [0, L]$ .

## References

- [1] B. A. Gregg, *J. Phys. Chem. B*, vol. 107, pp. 4688-4698, 2003.
- [2] G. D. Scholes, *ACS Nano*, vol. 2, pp. 523-537, 2008.
- [3] J. van de Lagemaat and A. J. Frank, *J. Phys. Chem. B*, vol. 104, pp. 4292-4294, 2000.
- [4] A. Kudo and Y. Miseki, "Heterogeneous photocatalyst materials for water splitting," *Chemical Society Reviews*, vol. 38, pp. 253-278, 2009.
- [5] T. O'Connor, M. S. Panov, A. Mereshchenko, A. N. Tarnovsky, R. Lorek, D. Perera, G. Diederich, S. Lambright, P. Moroz and M. Zamkov, "The Effect of the Charge-Separating Interface on Exciton Dynamics in Photocatalytic Colloidal Heteronanocrystals," *ACS Nano*, vol. 6, pp. 8156-8165, 2012.
- [6] K.-S. Mun, S. D. Alvarez, W.-Y. Choi and M. J. Sailor, "A Stable, Label-free Optical Interferometric Biosensor Based on TiO<sub>2</sub> Nanotube Arrays," *ACS Nano*, vol. 4, pp. 2070-2076, 2010.
- [7] N. R. Monahan, K. W. Williams, B. Kumar, C. Nuckolls and X.-Y. Zhu, "Direct Observation of Entropy-Driven Electron-Hole Pair Separation at an Organic Semiconductor Interface," *Physical Review Letters*, vol. 114, p. 247003, 2015.
- [8] M. T. Trinh, X. Wu, D. Niesner and X.-Y. Zhu, *Journal of Materials Chemistry A*, vol. 3, p. 9285, 2015.
- [9] P. Umari, E. Mosconi and F. De Angelis, *Scientific Reports*, vol. 4, p. 4467, 2014.
- [10] H. Wang and L. M. Peter, *J. Phys. Chem. C*, vol. 113, pp. 18125-18133, 2009.
- [11] T. Berger, J. A. Anta and V. Morales-Florez, "Spectroscopic properties of electrochemically populated electronic states in nanostructured TiO<sub>2</sub> films: anatase versus rutile," *Physical Chemistry Chemical Physics*, vol. 15, pp. 13790-13795, 2013.
- [12] P. Reckers, M. Dimamay, J. Klett, S. Trost, K. Zilberberg, T. Riedl, B. A. Parkinson, J. Brotz, W. Jaegermann and T. Mayer, *Journal of Physical Chemistry C*, vol. 119, pp. 9890-9898, 2015.
- [13] E. Hendry, M. Koeberg, B. O'Regan and M. Bonn, *Nano Lett.*, vol. 6, pp. 755-759,

2006.

- [14] E. Galoppini, J. Rochford, H. Chen, G. Saraf, Y. Lu, A. Hagfeldt and G. Boschloo, *J. Phys. Chem. B*, vol. 110, pp. 16159-16161, 2006.
- [15] E. Enache-Pommer, B. Liu and E. S. Aydil, *Phys. Chem. Chem. Phys.*, vol. 11, pp. 9648-9652, 2009.
- [16] E. Enache-Pommer, J. E. Boercker and E. S. Aydil, *Appl. Phys. Lett.*, vol. 91, pp. 123113-123116, 2007.
- [17] P. Docampo, S. Guldin, U. Steiner and H. J. Snaith, *J. Phys. Chem. Lett.*, vol. 4, p. 698, 2013.
- [18] S. K. Wallace and K. P. McKenna, *Adv. Mater. Interfaces*, vol. 1, p. 1400078, 2014.
- [19] Y. Furubayashi, N. Yamada, Y. Hirose, Y. Yamamoto, M. Otani, T. Hitosugi, T. Shimada and T. Hasegawa, *J. Appl. Phys.*, vol. 101, p. 093705, 2007.
- [20] A. C. Fisher, L. M. Peter, E. A. Ponomarev, A. B. Walker and K. G. U. Wijayantha, *J. Phys. Chem. B*, vol. 104, pp. 949-958, 2000.
- [21] L. M. Peter, *J. Phys. Chem. C*, vol. 111, pp. 6601-6612, 2007.
- [22] B. C. O'Regan and J. R. Durrant, *Acc. Chem. Res.*, vol. 42, pp. 1799-1808, 2009.
- [23] T. Berger, J. A. Anta and V. Morales-Flórez, *J. Phys. Chem. C*, vol. 116, p. 11444, 2012.
- [24] D. A. Panayotov, S. P. Burrows and J. R. Morris, *J. Phys. Chem. C*, vol. 116, p. 4535, 2012.
- [25] M. Chiesa, M. C. Paganini, S. Livraghi and E. Giamello, *Phys. Chem. Chem. Phys.*, vol. 15, p. 9435, 2013.
- [26] S. Livraghi, M. Chiesa, M. C. Paganini and E. Giamello, *J. Phys. Chem. C*, vol. 115, p. 25413, 2011.
- [27] C. Di Valentin, G. Pacchioni and A. Selloni, *Physical Review Letters*, vol. 97, p. 166803, 2006.
- [28] E. Finazzi, C. Di Valentin, G. Pacchioni and A. Selloni, *J. Chem. Phys.*, vol. 129, p. 154113, 2008.

- [29] C. Di Valentin, G. Pacchioni and A. Selloni, "Reduced and n-Type Doped TiO<sub>2</sub>: Nature of Ti<sup>3+</sup> species," *J. Phys. Chem. C*, vol. 113, pp. 20543-20552, 2009.
- [30] B. J. Morgan and G. W. Watson, *J. Phys. Chem. C*, vol. 114, pp. 2321-2328, 2010.
- [31] A. C. Papageorgiou, N. S. Beglitis, C. L. Pang, G. Teobaldi, G. Cabailh, Q. Chen, A. J. Fisher, W. A. Hofer and G. Thornton, *Proc. Natl. Acad. Sci. (USA)*, vol. 107, pp. 2391-2396, 2010.
- [32] N. A. Deskins, R. Rousseau and M. Dupuis, "Defining the Role of Excess Electrons in the Surface Chemistry of TiO<sub>2</sub>," *J. Phys. Chem. C*, vol. 114, pp. 5891-5897, 2010.
- [33] N. A. Deskins, R. Rousseau and M. Dupuis, *J. Phys. Chem. C*, vol. 115, pp. 7562-7572, 2011.
- [34] S. Chretien and H. Metiu, *J. Phys. Chem. C*, vol. 115, pp. 4696-4705, 2011.
- [35] T. Yamamoto and T. Ohno, *Phys. Chem. Chem. Phys.*, vol. 14, pp. 589-598, 2012.
- [36] K. Yang, Y. Dai, B. Huang and Y. P. Feng, *Phys. Rev. B*, vol. 81, p. 033202, 2010.
- [37] C. Di Valentin and A. Selloni, *J. Phys. Chem. Lett.*, vol. 2, pp. 2223-2228, 2011.
- [38] B. J. Morgan, D. O. Scanlon and G. W. Watson, *J. Mat. Chem.*, vol. 19, pp. 5175-5178, 2009.
- [39] P. Deak, B. Aradi and T. Frauenheim, *Phys. Rev. B*, vol. 83, p. 155207, 2011.
- [40] K. Yang, Y. Dai, B. Huang and Y. P. Feng, *J. Phys. D: Appl. Phys.*, vol. 47, p. 275101, 2014.
- [41] T. Yamamoto and T. Ohno, *Phys. Rev. B*, vol. 85, p. 033104, 2012.
- [42] A. Iwazuk and M. Nolan, *J. Phys. Chem. C*, vol. 115, p. 12995, 2011.
- [43] C. Di Valentin, E. Finazzi, G. Pacchioni, A. Selloni, S. Livraghi, M. C. Paganini and E. Giamello, *Chem. Phys.*, vol. 339, p. 44, 2007.
- [44] C. Di Valentin and G. Pacchioni, *Catal. Today*, vol. 206, pp. 12-18, 2013.
- [45] N. A. Deskins, R. Rousseau and M. Dupuis, *J. Phys. Chem. C*, vol. 113, pp. 14583-14586, 2009.



- [46] A. Janotti, C. Franchini, J. B. Varley, G. Kresse and C. G. Van de Walle, *phys. stat. sol. RRL*, vol. 3, pp. 199-203, 2013.
- [47] M. Setvin, C. Franchini, X. Hao, M. Schmid, A. Janotti, M. Kaltak, C. G. Van de Walle, G. Kresse and U. Diebold, *Phys. Rev. Lett.*, vol. 113, p. 086402, 2014.
- [48] H. Sezen, M. Buchholz, A. Nefedov, C. Natzeck, S. Heissler, C. Di Valentin and C. Wöll, *Sci. Rep.*, vol. 4, p. 3808, 2014.
- [49] C. Spreafico and J. VandeVondele, *Phys. Chem. Chem. Phys.*, vol. 16, p. 26144, 2014.
- [50] S. K. Wallace and K. P. Mckenna, *J. Phys. Chem. C*, vol. 119, pp. 1913-1920, 2015.
- [51] F. Nunzi, E. Mosconi, L. Storchi, E. Ronca, A. Selloni, M. Graetzel and F. De Angelis, *Energy Environ. Sci.*, vol. 6, p. 1221, 2013.
- [52] J. C. Garcia, M. Nolan and N. A. Deskins, *J. Chem. Phys.*, vol. 142, p. 024708, 2015.
- [53] M. Setvin, X. Hao, B. Daniel, J. Pavelec, Z. Novotny, G. S. Parkinson, M. Schmid, G. Kresse, C. Franchini and U. Diebold, *Angew. Chem. Int. Ed.*, vol. 53, pp. 4714-4716, 2014.
- [54] J. Zhang, T. F. Hughes, M. Steigerwald, L. Brus and R. A. Friesner, *J. Am. Chem. Soc.*, vol. 134, pp. 12028-12042, 2012.
- [55] R. Dovesi, R. Orlando, B. Civalleri, C. Roetti, V. P. Saunders and C. M. Zicovich-Wilson, *Z. Kristallogr.*, vol. 220, p. 571, 2005.
- [56] R. Dovesi, V. R. Saunders, C. Roetti, R. Orlando, C. M. Zicovich-Wilson, F. Pascale, B. Civalleri, K. Doll, N. M. Harrison, I. J. Bush, P. D'Arco and M. Llunell, "CRYSTAL09 User's Manual," University of Torino, Torino, 2009.
- [57] F. Corá, *Mol. Phys.*, vol. 103, pp. 2483-2496, 2005.
- [58] R. Dovesi, C. Roetti, C. Freyria Fava, M. Prencipe and V. R. Saunders, *Chem. Phys.*, vol. 156, pp. 11-19, 1991.
- [59] "CRYSTAL - Basis Sets Library," [Online]. Available: [http://www.crystal.unito.it/Basis\\_Sets/Ptable.html](http://www.crystal.unito.it/Basis_Sets/Ptable.html).
- [60] A. D. Becke, *Phys. Rev. A*, vol. 38, pp. 3098-3100, 1988.

- [61] C. Lee, W. Yang and R. G. Parr, *Phys. Rev. B*, vol. 37, pp. 785-789, 1988.
- [62] Z. Hu and H. Metiu, "Choice of U for DFT+U calculations for Titanium Oxides," *J. Phys. Chem. C*, vol. 115, pp. 5841-5845, 2011.
- [63] F. Aryasetiawan, K. Karlsson, O. Jepsen and U. Schönberger, *Phys. Rev. B*, vol. 74, p. 125106, 2006.
- [64] N. Martsinovich, D. R. Jones and A. Troisi, *J. Phys. Chem. C*, vol. 114, pp. 22659-22670, 2010.
- [65] T. Bredow, E. Aprà, M. Catti and G. Pacchioni, *Surf. Sci.*, vol. 418, p. 150, 1998.
- [66] T. Albaret, F. Finocchi, C. Noguera and A. De Vita, *Phys. Rev. B*, vol. 65, p. 035402, 2001.
- [67] C. L. Pang, C. A. Muryn, A. P. Woodhead, H. Raza, S. A. Haycock, V. R. Dhanak and G. Thornton, *Surf. Sci.*, vol. 583, p. L147, 2005.
- [68] P. Lagarde, A.-M. Flank, R. J. Prado, S. Bourgeois and J. Jupille, *Surf. Sci.*, vol. 553, p. 115, 2004.
- [69] F. Wegner, *Z. Physik B*, vol. 36, pp. 209-214, 1980.
- [70] N. C. Murphy, R. Wortis and W. A. Atkinson, *Phys. Rev. B*, vol. 83, p. 184206, 2011.
- [71] P. R. Rimbey, *Surf. Sci.*, vol. 85, p. 166, 1979.
- [72] N. A. Gippius, A. L. Yablonskii, A. B. Dzyubenko, S. G. Tikhodeev, L. V. Kulik, D. Kulakovskii and A. Forchel, *J. App. Phys.*, vol. 83, pp. 5410-5417, 1998.
- [73] J. Zhao, N. Pontius, A. Winkelmann, V. Sametoglu, A. Kubo, A. G. Borisov, D. Sánchez-Portal, V. M. Silkin, E. V. Chulkov, P. M. Echenique and H. Petek, *Phys. Rev. B*, vol. 78, p. 085419, 2008.
- [74] A. Gagliardi, S. Mastroianni, D. Gentilini, F. Giordano, A. Reale, T. M. Brown and A. Di Carlo, *Journal of Selected Topics in Organic Electronics*, vol. 16, pp. 1611-1618, 2010.
- [75] T. Sometani and K. Hasebe, "Method for solving electrostatic problems having a simple dielectric boundary," *Am. J. Phys.*, vol. 45, p. 918, 1977.
- [76] A. B. Dzyubenko and A. L. Yablonskii, *Phys. Rev. B*, vol. 53, p. 16355, 1996.

- [77] J. Karwowski and M. Stanke, *Struct. Chem.*, vol. 15, pp. 427-429, 2004.
- [78] W. H. Press, S. A. Teukolsky, W. T. Vetterling and B. P. Flannery, *Numerical Recipes in FORTRAN 90*, 2nd ed., Cambridge University Press, 1997.
- [79] G. A. Acket and J. Volger, *Physica*, vol. 32, p. 1680, 1966.
- [80] J. Pascual, J. Camassel and H. Mathieu, *Phys. Rev. Lett.*, vol. 39, p. 1490, 1977.
- [81] C. Kormann, D. W. Bahnemann and M. R. Hoffmann, *J. Phys. Chem.*, vol. 92, pp. 5196-5201, 1988.
- [82] B. Enright and D. Fitzmaurice, *J. Phys. Chem.*, vol. 100, pp. 1027-1035, 1996.
- [83] H. P. R. Frederikse, *J. Appl. Phys.*, vol. 32, p. 2211, 1961.
- [84] J. Yahia, *Phys. Lett.*, vol. 23, p. 425, 1966.
- [85] H. Tang, K. Prasad, R. Sanginès, P. E. Schmid and F. Lévy, *J. Appl. Phys.*, vol. 75, p. 2042, 1994.
- [86] M. D. Stamate, "On the non-linear I-V characteristics of dc magnetron sputtered TiO<sub>2</sub> thin films," *Appl. Surf. Sci.*, vol. 205, pp. 353-357, 2003.
- [87] C. E. Ekuma and D. Bagayoko, *Jpn. J. Appl. Phys.*, vol. 50, p. 101103, 2011.
- [88] T. Le Bahers, M. Rérat and P. Sautet, *J. Phys. Chem. C*, vol. 118, pp. 5997-6008, 2014.
- [89] H. A. Huy, B. Aradi, T. Frauenheim and P. Deák, *Phys. Rev. B*, vol. 83, p. 155201, 2011.
- [90] R. A. Parker, *Phys. Rev.*, vol. 124, pp. 1719-1722, 1961.
- [91] W. G. Lee, S. I. Woo, J. C. Kim, S. H. Choi and K. H. Oh, *Thin Solid Films*, vol. 105, p. 237, 1994.
- [92] M. D. Stamate, "On the dielectric properties of dc magnetron TiO<sub>2</sub> thin films," *Appl. Surf. Sci.*, vol. 218, pp. 317-322, 2003.
- [93] G. Ritzoulis, N. Papadopoulos and D. Jannakoudakis, *J. Chem. Eng. Data*, vol. 31, pp. 146-148, 1986.

- [94] B. E. Conway, J. O. Bockris and I. A. Ammar, *Trans. Faraday Soc.*, vol. 47, pp. 756-766, 1951.
- [95] C. M. Yim, C. L. Pang and G. Thornton, *Phys. Rev. Lett.*, vol. 104, p. 036806, 2010.
- [96] S. Varaganti and G. Ramakrishna, *J. Phys. Chem. C*, vol. 114, pp. 13917-13925, 2010.
- [97] G. Onida, L. Reining and A. Rubio, "Electronic excitations: density-functional versus many-body Green's-function approaches," *Rev. Mod. Phys.*, vol. 74, pp. 601-659, 2002.
- [98] P. Cudazzo, F. Sottile, A. Rubio and M. Gatti, "Exciton dispersion in molecular solids," *J. Phys.: Condens. Matter*, vol. 27, p. 113204, 2015.
- [99] Q. X. Yang, M. Muntwiler and X. Y. Zhu, *Phys. Rev. B*, vol. 80, p. 115214, 2009.